ACS Catalysis

pubs.acs.org/acscatalysis Research Article

Directed Mass and Electron Transfer Promoted by Hierarchical Porous Co−P−O Leads to Enhancement of the Overall Water Splitting Efficiency

Jiang-Bo Chen, Jie Ying,* Yu-Xuan Xiao, Ge Tian, Yuan Dong, Ling Shen, Susana I. Córdoba de Torresi, Mark D. Symes, Christoph Janiak, and Xiao-Yu Yang*

Cite This: *ACS Catal.* 2023, 13, 14802−14812 Read Online

ABSTRACT: Optimization of the efficiencies of both macroscale mass transport and microscale electron transfer is highly desired for achieving high-performance electrocatalysts but still remains a great challenge. Herein, a facile topological conversion method is developed to synthesize a novel O-incorporated CoP derivative (denoted as Co−P−O) with directed mass and electron transfer effects, which benefits from its hierarchical porous structure and internal atomic n-p homojunction, respectively. As a result, Co−P−O achieves optimal hydrogen evolution reaction (HER) and oxygen evolution reaction (OER) performance with low overpotentials (113 and 256 mV at 10 mA cm^{-2}, respectively) and enhanced durability in water splitting. Density functional theory calculations further reveal that both the degree of polarization/rearrangement of the overall surface charge and the delocalization effects of the d electrons of Co−P−O are enhanced, leading to optimal adsorption of H_2O/OH^- and desorption of the generated gases for enhancing HER and OER activities.

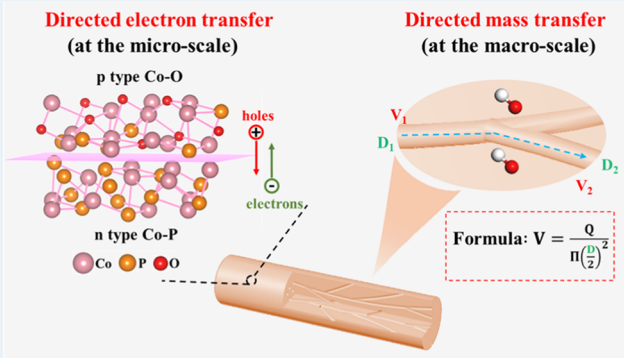

KEYWORDS: *metal phosphides, hierarchical porous structure, homojunction, directed transfer, overall water splitting*

■ INTRODUCTION

Electrocatalysis plays a central role as a sustainable technology for green hydrogen production (from renewable electricity) through the hydrogen evolution reaction (HER) and oxygen evolution reaction (OER) forming the two events/half-reactions of electrocatalytic water splitting.[1] Two key features of electrocatalytic water splitting are liquid-phase mass transfer (involving adsorption and desorption of substrates and reactive intermediates) and electron transfer at the anode and cathode interfaces.[2−4] The efficiencies of both processes are highly dependent on the properties of the electrochemical catalysts.[5,6] Thus, an important goal guiding the design of new high-performance electrocatalyst systems is the optimization of macroscale mass transport via effective strategies, such as constructing hierarchical porosity, nanostructuring engineering, dealloying, etc.,[7,8] by amplifying diffusion and increasing the probability for contact with the active sites or by altering the hydrophilicity and surface tension.[9−11] In addition, optimization of the efficiency of microscale electron transport can be obtained via modulating electron structures, such as element doping, defect engineering, interface constructing, etc.,[12,13] by selecting electrode materials in which orbital coupling, molecular symmetry, and orbital degeneracy are optimal.[14−16]

The search for materials with rapid mass transfer proficiencies has uncovered hierarchically porous structures that contain both abundant internal mass transfer channels and active sites exposed on the inner surface. For example, Yu et al. demonstrated that hierarchically porous channels in Pt nanotubes, in which overlap of the electric double layer is avoided, greatly promote the transfer of reactive substances from the bulk electrolyte to the electric double layer on the surface of the catalyst.[17] In addition, we recently devised a simple galvanic replacement method for the preparation of efficient and durable hierarchical fractal PtPdCu sponges, containing three-dimensional hierarchical fractal pores, which facilitate the transport of reactants from large to small pores.[18] We also demonstrated that this material serves as a high-performance electrocatalyst in methanol electro-oxidation. However, the synthesis of this hierarchical porous structure is cumbersome, and it leads to the loss of catalytic active sites.

Received: August 28, 2023
Revised: October 17, 2023
Accepted: October 18, 2023

https://doi.org/10.1021/acscatal.3c04067
ACS Catal. 2023, 13, 14802−14812

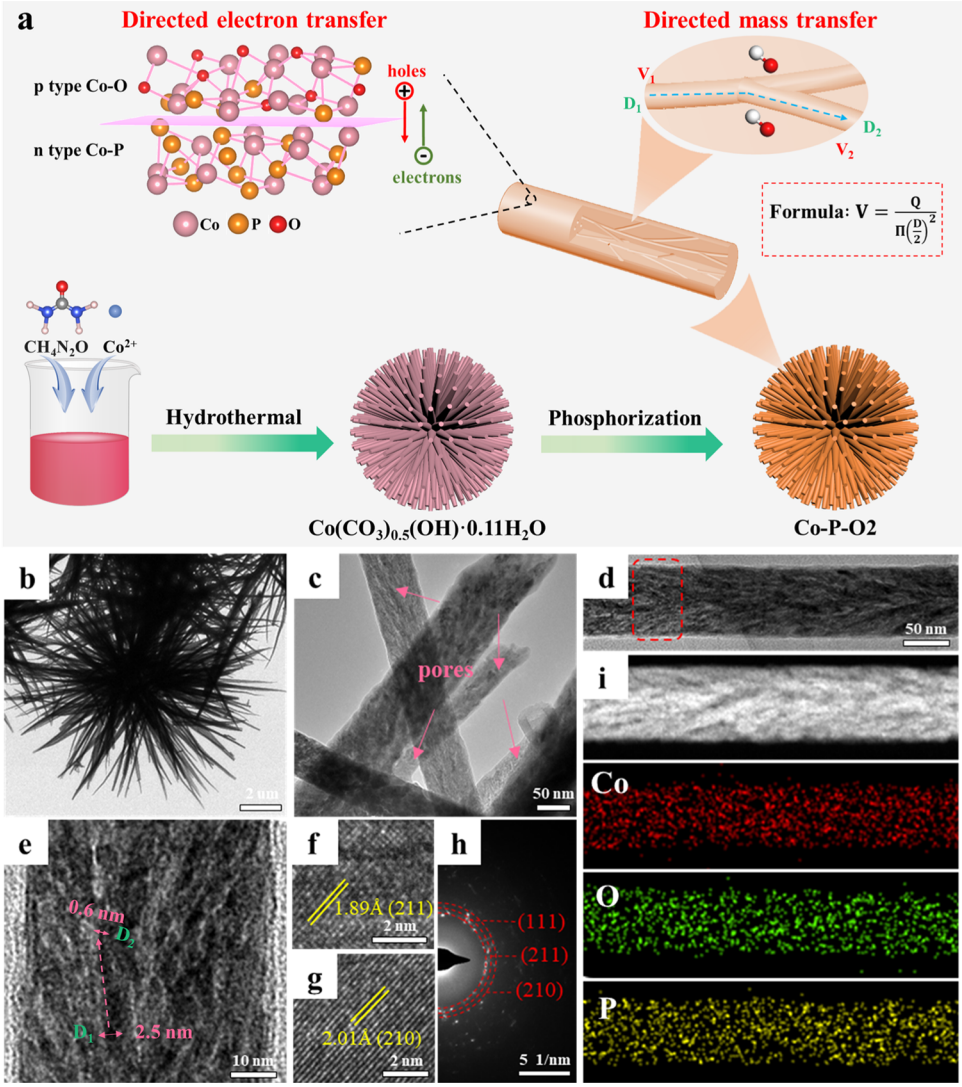

Figure 1. (a) Schematic illustration of the intrinsic mechanisms for matter and electron transport in Co−P−O and a scheme of the synthesis of Co−P−O nanocrystals. (b−e) TEM images of Co−P−O2 with different magnifications. (f, g) HRTEM images of Co−P−O2. (h) SAED pattern of Co−P−O2. (i) HAADF-STEM image of Co−P−O2 and corresponding EDX elemental mapping results.

Thus, a simple method for the fabrication of hierarchical porous structures without destroying the original active sites is in high demand.

Investigations focused on enhancing electron transfer in electrocatalytic systems have shown that the presence of n-p junctions leads to an acceleration of electron transfer because of their ability to create a built-in electric field that promotes directed charge transfer.[19,20] Directed electron transfer at the interfaces of n-p junctions elevates the adsorption energies of key intermediates[21] in the catalytic reactions and reduces the internal energy barrier of electrochemical reactions.[22] In one effort, Xu and co-workers constructed a CuO@CoOOH n-p heterojunction, which had significantly altered electronic properties in the space charge region that led to the promotion of electron transfer.[23] Also, Qian et al. synthesized a semiconductor p−n junction, consisting of a p-type CoP array and an n-type FeNi-LDH nanosheet that served as a catalytically active center, in which the electronic structure of the space charge region of the active site was regulated.[19] However, the nature of an n-p heterojunction is governed by properties, such as band gap arrangement, crystal structure, and lattice parameters, as well as other characteristics. In contrast, electron transfer is more favorable at homogeneous n-p junctions in a single material with continuous band bending.[24] Owing to the heterogeneity of charge regions in n/p semiconductors, directed electron transfer at the atomic scale is exceedingly difficult to regulate.

Studies carried out in the past, which were influenced by the above considerations, revealed that cobalt phosphide (CoP) is a universal nonprecious metal-based electrocatalyst, especially for the water splitting process.[10,25,26] In the effort described below, we prepared and evaluated the electrocatalytic performance of a new O-incorporated CoP derivative, denoted as Co−P−O. We observed that this material, which is fabricated using a facile topological conversion method, has a hierarchical porous structure that enables fast mass transfer through constructing hierarchical porosity and n-p homojunctions between the n-type region of Co−P and the p-type region of Co−O, forming a new built-in electric field for directed electron transfer. The results of electrochemical investigations indicate that the extent of O incorporation in Co−P−O has a remarkable effect on the efficiencies of both the HER and

https://doi.org/10.1021/acscatal.3c04067
ACS Catal. 2023, 13, 14802−14812

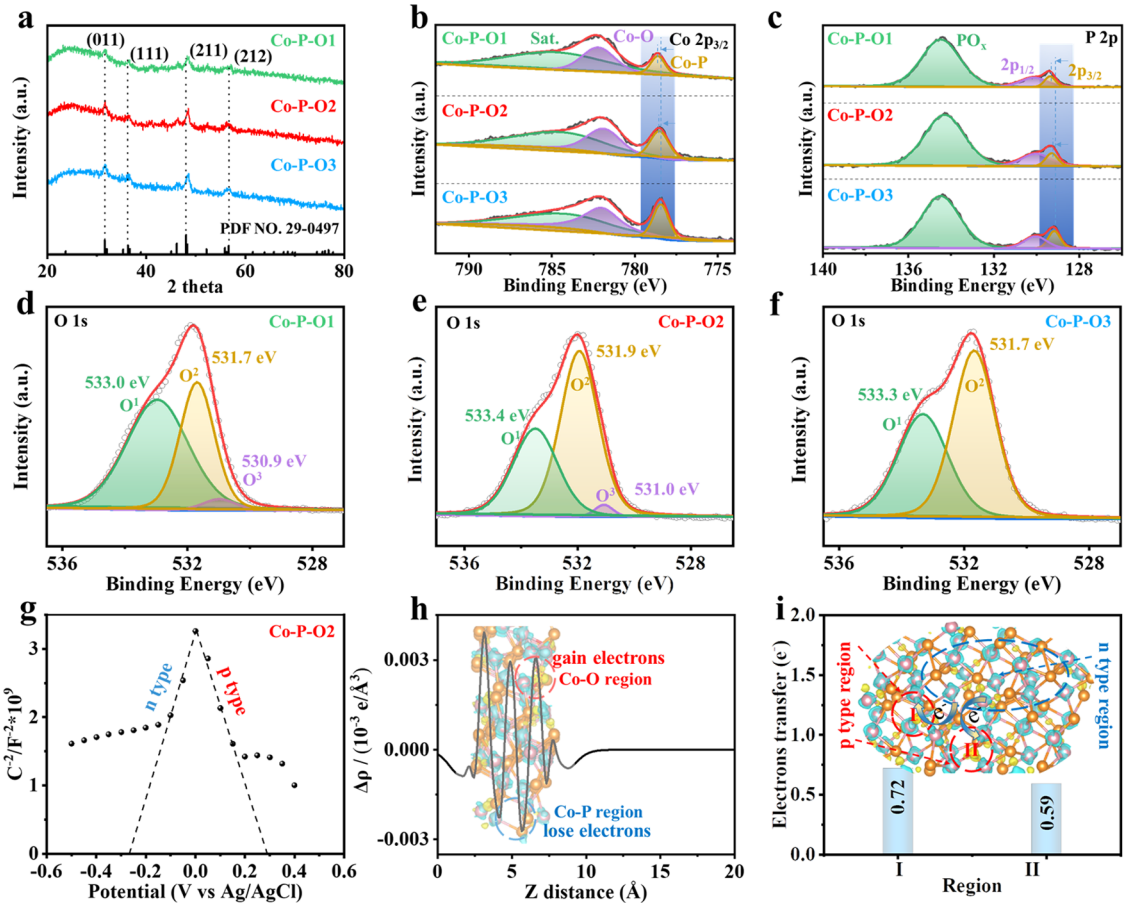

Figure 2. (a) XRD patterns and (b) high-resolution XPS spectra of Co $2p_{3/2}$, (c) P 2p, and (d−f) O 1s for Co−P−O1, Co−P−O2, and Co−P−O3. (g) Mott−Schottky plots of Co−P−O2 according to impedance measurements. (h) Planar-average charge density and (i) n/p-type region electron transfer of Co−P−O2 (yellow region indicates charge accumulation; cyan region indicates charge depletion).

OER. The as-synthesized Co−P−O exhibits excellent electrocatalytic performance for both alkaline HER and OER with small overpotentials (η_{10}, at 10 mA cm^{-2}) of only 113 and 256 mV, respectively. Overall water splitting can be stably delivered at a low η_{10} cell voltage of 1.67 V, and the system exhibits extraordinary stability over a continuous operation for 20 h. Density functional theory (DFT) simulation supports the experimental results by demonstrating that an appropriate level of oxygen incorporation effectively improves electrical conductivity, enhances d-electron delocalization on the Co atom close to the O atom, and modulates the electronic structure of CoP. We anticipate that the present design strategy for directed transport of mass and electrons will offer new insights to design high-efficiency electrocatalysts for energy conversion devices.

■ RESULTS AND DISCUSSION

The conceptual basis for elevated directed mass and electron transfer that we propose to occur in Co−P−O is schematically represented in the top part of Figure 1a. Because the pore sizes in the branches are smaller than those in the trunk ($D_2 < D_1$) of this material, we anticipated that directed mass transfer will be promoted by the change occurring in the electrolyte diffusion rate in the small branches (V_2) versus the trunk (V_1) according to the fluid formula $V = Q/\pi(D/2)^2$, where V, Q, and D are the respective transfer velocity, flow rate, and diameter of the pores.[18] The resulting directed mass transfer of the electrolyte from the branches to the trunks could facilitate maximum exploitation of inner active sites. In addition, a difference exists between the band structures in the n-type Co−P regions and p-type Co−O regions at the atomic level in Co−P−O, enhancing electron utilization efficiency and activating reactive Co atoms for better adsorption/desorption ability accelerating the catalytic process.

A scheme for the preparation of hierarchically porous Co−P−O nanocrystals with different oxygen contents is displayed in Figure 1a. The $Co(CO_3)_{0.5}(OH)\cdot 0.11H_2O$ precursor employed in the synthetic pathway was generated via simple hydrothermal growth in a mixture of $CoCl_2\cdot 6H_2O$ and urea. Formation of the target compound in this process is likely initiated by the decomposition of urea ($CO(NH_2)_2 + 3H_2O \rightarrow 2NH_4^+ + CO_2 + 2OH^-$). The X-ray diffraction (XRD) pattern of this substance (Figure S1) correlates with that of orthorhombic $Co(CO_3)_{0.5}(OH)\cdot 0.11H_2O$ (PDF#48-0083). Scanning electron microscopy (SEM) images of prepared $Co(CO_3)_{0.5}(OH)\cdot 0.11H_2O$ (Figure S2a,b) show that individual branches are tens of microns in length. Precipitated $Co(CO_3)_{0.5}(OH)\cdot 0.11H_2O$ was then phosphatized using NaH_2PO_2 in different times and atmospheres. This process produces Co−P−O containing different oxygen contents denoted as Co−P−O1, Co−P−O2, and Co−P−O3 (see the Experimental Section in the SI). Notably, the Co−P−O nanocrystals have hierarchical porous structures caused by the release of H_2O and CO_2 during the high-temperature process. Also, they possess atomic-level n-p homojunctions as a result

https://doi.org/10.1021/acscatal.3c04067
ACS Catal. 2023, 13, 14802−14812

of modifications of the electronegativity and coordination environment of Co promoted by oxygen doping.

Figure S3 shows SEM images of multiple and single nanocrystals of Co−P−O, which have the same morphology as the $Co(CO_3)_{0.5}(OH)\cdot 0.11H_2O$ precursor. Moreover, the transmission electron microscopy (TEM) images displayed in Figure 1b−e reveal that the nanocrystals have branches, composed of many hierarchical pores and stomatal channels in Co−P−O2, where pores in the trunk are broader (2.5 nm) than those in the branches (0.6 nm). Moreover, the TEM images of branches in single nanocrystals of Co−P−O2 show that they have a wedge-shaped structure with a width of ∼40 nm at the top and ∼80 nm at the bottom (Figure S4). As per the fluid formula described in Figure 1a, these size differences could result in the directed mass transfer of the electrolyte from branches to trunks, facilitating the maximum exploitation of inner active sites. High-resolution TEM (HRTEM) images (Figure 1f,g) confirm that Co−P−O2 has interplane distances at the lattice fringes of 0.189 and 0.201 nm, which correspond to the (211) facet and (210) facet of CoP (PDF#29-0497), respectively. The corresponding selected area electron diffraction (SAED) pattern of Co−P−O2 (Figure 1h) shows that it has a typical polycrystalline nature composed of nanocrystals with three predominant diffraction rings, which can be indexed to the (111), (210), and (211) atomic planes of CoP. A high-angle annular dark field (HAADF) image and a corresponding elemental mapping (Figure 1i) show that Co, P, and O are spatially distributed in a well-defined manner.

The phase structures of the hierarchically porous Co−P−O nanocrystals were initially examined by XRD (Figure 2a). The results clearly show that the precursor is converted by phosphorization into orthorhombic CoP, where the Co atom is coordinated with six P atoms. Moreover, because the electronegativity of Co (1.88) has a different gap from that of O (3.44) and P (2.19), the O atoms entering the CoP lattice will lead to changes in the local environment of the material (such as bond length, bond angle) and in the overall electronic structure of the material.[27] Furthermore, X-ray photoelectron spectroscopy (XPS) was employed to gain further information about the atomic composition and the oxidation states at the surface of Co−P−O containing different oxygen contents, where the survey spectrum of Co−P−O2 shows the existence of Co, P, and O (Figure S5). The high-resolution XPS spectra of Co $2p_{3/2}$, P 2p, and O 1s are shown in Figure 2b−f. The Co $2p_{3/2}$ region contains peaks at 781.9 and 785.2 eV associated with oxidized species and satellite peaks in Co−P−O2, along with peaks at 782.2 and 785.3 eV corresponding to Co−P−O1, and 782.1 and 785.1 eV associated with Co−P−O3.[28] The peak at 778.5 eV in the Co $2p_{3/2}$ XPS region of the spectrum of Co−P−O2 is higher in energy than that of Co−P−O3 (778.4 eV) but lower than that of Co−P−O1 (778.6 eV) (Figure 2b).[3] This observation indicates that the electron density at Co is redistributed upon increasing the incorporation of O, leading to a relatively more positively charged Co center for the promotion of adsorption/desorption of intermediates. Specifically, the more positively charged Co center could optimize the electron configuration of the e_g orbital filling, balancing the binding energy between the catalytic site and involved oxygen intermediates (OH*, O*, and OOH*) for OER.[29] At the same time, it could also change the d orbital electron state of Co and then regulate its interaction with the s orbital of intermediate (H*) for HER.[30] Hence, the desorption and adsorption behaviors of different reactions were optimized. In the XPS spectral region corresponding to P 2p, two distinct peaks associated with Co−P−O2 are present at 129.3 and 130.0 eV, whereas the peaks at 129.4 and 130.1 eV are linked to Co−P−O1, and those at 129.2 and 129.9 eV are associated with Co−P−O3 (Figure 2c).[10] In addition, the peak at 134.3 eV in the P 2p region of the spectrum of Co−P−O2 represents an oxidized P species such as PO_4^{3-} formed upon air exposure, and those in the spectra of Co−P−O1 (134.5 eV) and Co−P−O3 (134.4 eV) are also linked to oxidized P species.[31] These findings show that the introduction of O induces an increase in the valence state of P, which suggests the transfer of electrons from phosphorus to oxygen. As can be seen by inspecting Figure 2d−f, the O 1s regions of the high-resolution XPS spectra of Co−P−O1 and Co−P−O2 contain typical oxygen-associated peaks denoted as O^1, O^2, and O^3, while that of Co−P−O3 only contains two groups of O^1 and O^2 peaks. Specifically, the O^1 peaks at 533.0, 533.4, and 533.3 eV are linked to physisorbed and chemisorbed water near the surface and the O^2 peaks at 531.7, 531.9, and 531.7 eV are typically associated with oxygen in OH^- groups at the surface.[28] The components of O^3 at 530.9 eV for Co−P−O1 and 531.0 eV for Co−P−O2 are associated with metal−oxygen bonds, indicating that oxygen still exists after phosphorization.[32] In contrast, the observation that the O 1s region in the spectrum of Co−P−O3 does not contain a characteristic O^3 peak shows that pure CoP exists as a result of complete phosphorization of $Co(CO_3)_{0.5}(OH)\cdot 0.11H_2O$. To obtain the oxygen contents of Co−P−O formed by phosphorization, ratios of the areas of the O^1, O^2, and O^3 peaks in the O 1s region of spectra of Co−P−O1 and Co−P−O2 were determined. The results show that 3.2% and 2.1% oxygen are present in metal−oxygen bonds in Co−P−O1 and Co−P−O2, respectively (Tables S1 and S2). Based on the results of XPS and inductively coupled plasma-atomic emission spectrometry (ICP-AES) (Table S3), the atomic ratios of Co, P, and O for Co−P−O1, Co−P−O2, and Co−P−O3 are approximately 50:46.8:3.2, 50:47.9:2.1, and 50:50:0, respectively. In addition, N_2 absorption−desorption isotherm plots of Co−P−O2 show typical type-II isotherm features and the Brunauer−Emmett−Teller (BET) surface area is 117.9 $m^2\ g^{-1}$ (Figure S6a). This suggests the possible presence of ink bottles or tubular holes, which is consistent with our TEM observations. Also, analysis using the Barret−Joyner−Halenda method shows that the pores in this material have mesoporous sizes (Figure S6b), suggesting that the pores will facilitate the diffusion of reactants into the inner surface to achieve directed mass transfer, which is consistent with the analysis results of TEM.

The interfacial charge behavior of Co−P−O2 was explored using Mott−Schottky (MS) plots and employing CoP (without introduction of O) and Co_3O_4 (without introduction of P) as references (Figures 2g and S7). The results show that Co_3O_4 exhibits p-type semiconductor behavior, while Co−P−O3 has n-type semiconductor properties (Figure S7), which are consistent with previous reports.[33,34] In contrast, MS results show that Co−P−O2 possesses both n-type and p-type properties (Figure 2g), where these properties endow Co−P−O2 with inner electric potentials, creating a new built-in electric field and suggesting that an inner n-p effect exists in the material, which would facilitate directed electron transport.[35] To further investigate the influence of oxygen incorporation on electronic properties of Co−P−O2, planar-average charge densities and Bader charges were calculated by utilizing DFT. Based on the XRD and TEM results, the (211) plane was used

https://doi.org/10.1021/acscatal.3c04067
ACS Catal. 2023, 13, 14802−14812

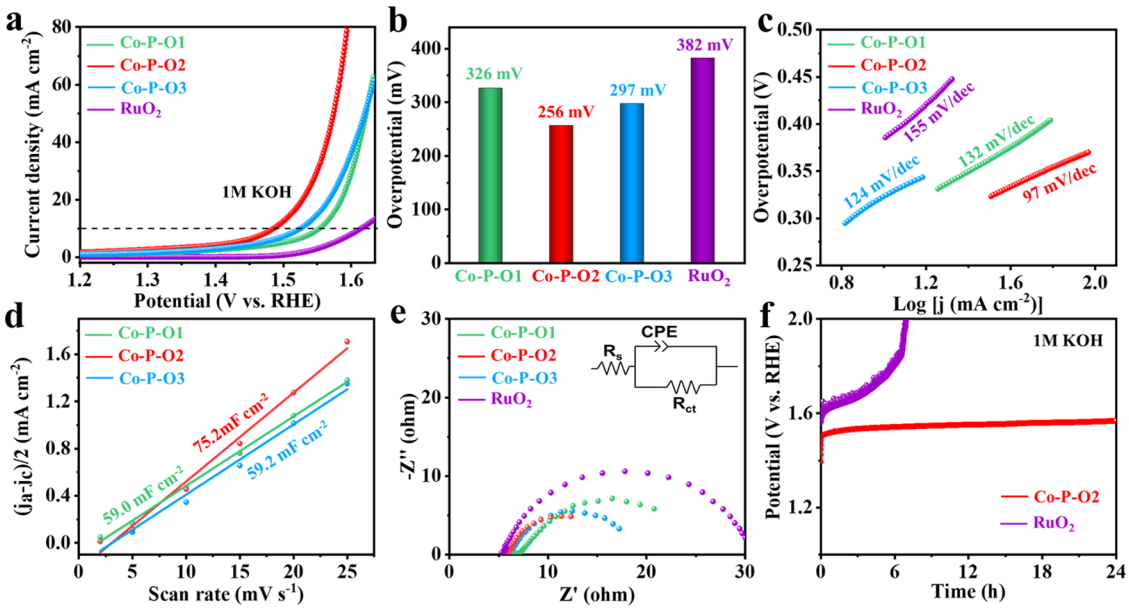

Figure 3. Electrocatalytic OER performance of different catalysts in a N_2-saturated 1.0 M KOH electrolyte. (a) LSV polarization curves at a scan rate of 5 mV s^{-1}, (b) overpotentials at a current density of 10 mA cm^{-2}, (c) Tafel slopes, (d) estimated C_{dl} values, and (e) Nyquist plots of as-prepared materials measured at 1.53 V and corresponding analog circuit. (f) Chronopotentiometry curves at a constant current density of 10 mA cm^{-2} in OER catalyzed by Co−P−O2 and RuO_2.

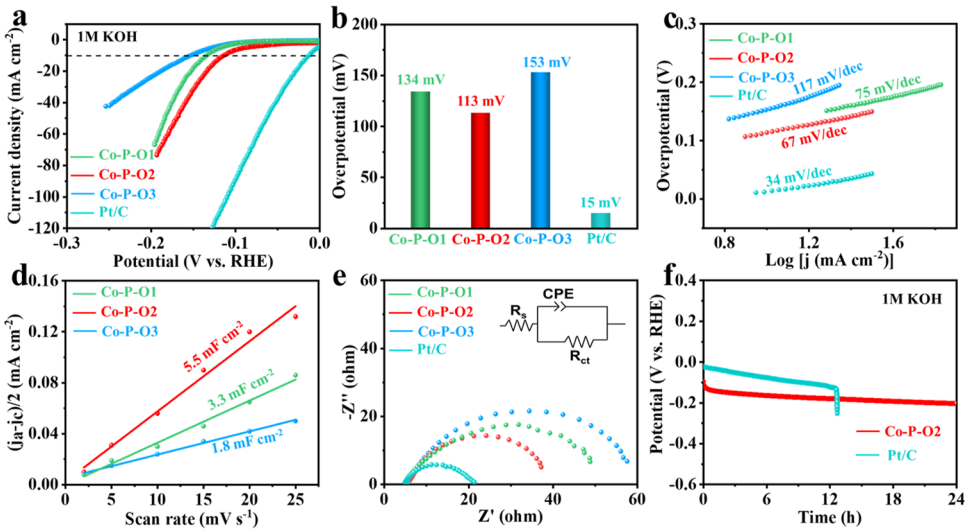

Figure 4. Electrocatalytic HER performance of different catalysts in a N_2-saturated 1.0 M KOH electrolyte. (a) LSV polarization curves at a scan rate of 5 mV s^{-1}, (b) overpotentials at a current density of 10 mA cm^{-2}, (c) Tafel slopes, (d) estimated C_{dl} values, and (e) Nyquist plots measured at −1.13 V of as-prepared materials and corresponding analog circuit. (f) Chronopotentiometry curves at a constant current density of 10 mA cm^{-2} in HER of Co−P−O2 and commercial Pt/C.

to model pristine CoP, and XPS results guided the construction of the model for Co−P−O2 (Figure S8). The results show that the charge density is polarized along the *Z*-axis and that electron enrichment is larger in the n-type Co−O region, again suggesting that the directed transfer of electrons could occur (Figure 2h). Bader charge analysis (Figure 2i) was conducted to determine the overall charge gain and loss in regions (I and II), where O exists in Co−P−O2 (Figure 2i, inset). The results reveal that regions I and II gain 0.72 and 0.59 electrons, respectively, which is consistent with the planar-average charge density results displayed in Figure 2h. The above results demonstrate that atomic n-p homojunctions exist in Co−P−O2.

The electrocatalytic activities of as-prepared Co−P−O2, along with control materials, including Co−P−O1, Co−P−O3, and commercial RuO_2, were determined in alkaline aqueous solutions by using a typical three-electrode electrochemical system. All potentials were referenced to the reversible hydrogen electrode. The linear sweep voltammetry (LSV) curves in Figure 3a show that among the four catalysts, Co−P−O2 exhibits the best OER performance in aqueous KOH (1.0 M) at 10 mA cm^{-2}. Also, the overpotential for the OER at 10 mA cm^{-2} (Figure 3b) of Co−P−O2 is 256 mV, which is much smaller than those of Co−P−O1 (326 mV), Co−P−O3 (297 mV), and RuO_2 (382 mV). Interestingly, the performance of Co−P−O1 is better than that of Co−P−O3 at

https://doi.org/10.1021/acscatal.3c04067
ACS Catal. 2023, 13, 14802−14812

a low potential, while the performance of Co−P−O3 is better than that of Co−O−P1 at a high potential, which may be ascribed to the adverse reconstruction of Co−P−O1 by increasing the potential.[36] This phenomenon may result from the relatively faster increase in the dynamic barrier or decrease in the number of exposed reaction centers for Co−P−O1 in comparison with Co−P−O3 at a high potential. Notably, the OER overpotential of Co−P−O2 is among those of state-of-the-art non-noble metal-based catalysts in the previous reports (Table S4). The Tafel slope of Co−P−O2 is 97 mV dec^{-1} (Figure 3c), which is smaller than those of Co−P−O1 (132 mV dec^{-1}), Co−P−O3 (124 mV dec^{-1}), and benchmark RuO_2 (155 mV dec^{-1}). The small Tafel slope of Co−P−O2 could aid practical applications, because it indicates that only a small overpotential increase is required to obtain a higher current density,[37−39] demonstrating the kinetic merit for the OER. In addition, analysis of cyclic voltammograms (CVs) outside the Faradaic regions, generated using different scan rates (Figures 3d and S9), shows that Co−P−O2 has a double-layer capacitance (C_{dl}) value of 75.2 mF cm^{-2}, which is noticeably larger than those of Co−P−O1 (59.0 mF cm^{-2}) and Co−P−O3 (59.2 mF cm^{-2}), implying that Co−P−O2 has a higher electrochemically active surface area (ECSA) (Figure S10). Evaluation of the conductivity and resistivity of all samples was carried out using electrochemical impedance spectroscopy (EIS) (Figure 3e), where the analog circuit from Nyquist plots suggests a smaller impedance and faster reaction rate (Table S5), indicating that Co−P−O2 has the smallest charge transfer resistance (R_{ct}) among all tested materials, which may be attributed to the appropriate O doping that regulates the CoP surface electronic structure.[40] Hence, it accelerated an interfacial electron transfer, suggesting that Co−P−O2 has a higher intrinsic catalytic activity for the OER in the alkaline electrolyte than the control materials, consistent with the calculated turnover frequency (TOF) at an overpotential of 300 mV of 3.77×10^{-3} s^{-1}, which is greater than that of RuO_2 (Table S6). Generally, the higher TOF can accelerate the mass transport process during the OER, resulting in the enhancement of electrocatalytic activity.[41] Moreover, chronopotentiometric (CP) measurements of Co−P−O2 during the OER for 24 h at a current density of 10 mA cm^{-2} (Figure 3f) show that an insignificant loss in activity occurs in comparison to commercial RuO_2, which demonstrates that Co−P−O2 has excellent stability.

The HER performance of Co−P−O2 and the other catalysts under alkaline conditions was also evaluated. The LSV curves of the catalysts (Figure 4a) demonstrate that Co−P−O2 exhibits excellent catalytic activity for the HER at 10 mA cm^{-2}. For quantitative comparison, the overpotentials at 10 mA cm^{-2} are extracted as shown in Figure 4b, where the overpotential of Co−P−O2 in the HER is 113 mV, which is lower than those of Co−P−O1 (134 mV) and Co−P−O3 (153 mV). Also, the HER overpotential of Co−P−O2 is among those for state-of-the-art non-noble metal-based catalysts in previous reports (Table S7). Figure 4c shows that the Tafel slope of Co−P−O2 (67 mV dec^{-1}) is smaller than those of Co−P−O1 (75 mV dec^{-1}) and Co−P−O3 (117 mV dec^{-1}), demonstrating that it has superior kinetics for the HER. According to the corresponding CVs with different scan rates outside the Faradaic regions, which are shown in Figure S11, Co−P−O2 exhibits a higher C_{dl} value (5.5 mF cm^{-2}) compared to Co−P−O1 (3.3 mF cm^{-2}) and Co−P−O3 (1.8 mF cm^{-2}), indicating that it has more ECSA (Figures 4d, S12). Furthermore, Co−P−O2 has a lower R_{ct} than Co−P−O1 and Co−P−O3 (Figure 4e, Table S8), which suggests that it displays faster charge transfer due to the optimized O doping content and interfacial electron structure.[42] The TOF value of Co−P−O2 in the HER process is 4.60×10^{-3} s^{-1} (at η = 120 mV), which is considerably larger than those of Co−P−O1 and Co−P−O3 (Table S9), contributing to the quick diffusion of the electrolyte during the HER. Additionally, Co−P−O2 displays a constant current output of 10 mA cm^{-2} (Figure 4f), showing an insignificant increment compared with that of commercial Pt/C through CP measurements.

To determine if the properties described above would lead to possible practical applications, a Co−P−O2 ‖ Co−P−O2 electrode couple was constructed for total water splitting in 1.0 M KOH. The stability of this dual electrode for water electrolysis in 1.0 M KOH is well maintained over 20 h of continuous operation at 1.67 V (Figure S13). Furthermore, the Faradaic efficiency of Co−P−O2 was evaluated using an H-style electrolytic cell at 35 mA cm^{-2} in 1.0 M KOH. As seen in Figures S14−16 and Table S10, the volumetric ratio of cathodic generative gas (H_2) to anodic one (O_2) matches well with the theoretical value (2:1), where the Faradaic efficiency of Co−P−O2 in overall water splitting was measured to be 98.8%. In addition, electrochemical tests were carried out in alkaline simulated seawater (1.0 M KOH + 3.5% NaCl) to assess applications of the Co−P−O2 catalyst for direct electrolytic hydrogen production from seawater (Figure S17). Results of these studies show that Co−P−O2 exhibits a performance for the OER and HER in alkaline simulated seawater that is much higher than those of Co−P−O1 and Co−P−O3 (Figure S17a,b). Also, EIS analysis shows that Co−P−O2 has a much lower charge transfer resistance than Co−P−O1 and Co−P−O3 (Figure S17c,d). Finally, CP measurements demonstrate that Co−P−O2 maintains its stability in both the OER and the HER for 10 h (Figure S17e,f).

Information about structural changes in Co−P−O2 that occur during long-term electrochemical reactions came from the results of SEM, XRD, XPS, and ICP-AES. Interestingly, the SEM images show that clear morphological changes for Co−P−O2 take place after its prolonged utilization in promoting both the OER and HER (Figure S13, inset). Specifically, during the HER, Co−P−O2 nanorods are converted to nanosheets, while they are converted to nanoplates during the OER. In addition, XRD analysis shows that the crystalline structure of Co−P−O2 undergoes a clear change during the OER and HER (Figure S18). We speculate that oxidation at a high potential in the OER leads to a change in which the surface of Co−P−O2 becomes amorphous or weakly crystalline, such as amorphous hydroxyl oxides. They may facilitate oxygen-bridged Co^{IV}−O−Co^{IV} moieties forming as the real active sites of the as-prepared Co−P−O2 when undergoing stepwise structural reconstructions during the OER.[25,43] The leaching of P during the HER leads to OH^- immersion that induces a phase transformation, such as hydroxide, which also may be the real active species during the HER and has been reported previously.[25,44] Specifically, the bias potential may boost the process of reconstruction, where P leaching urges Co−P−O2 to be chalked into P−Co−O−Co−P configurations with low-valence metal centers. Furtherly, the completely reconstructed catalyst with low crystallinity $Co(OH)_2$ nanosheets may lower the energy barrier for water dissociation and facilitate the adsorption/desorption of HER intermediates, thus accelerating the HER process.

https://doi.org/10.1021/acscatal.3c04067
ACS Catal. 2023, 13, 14802−14812

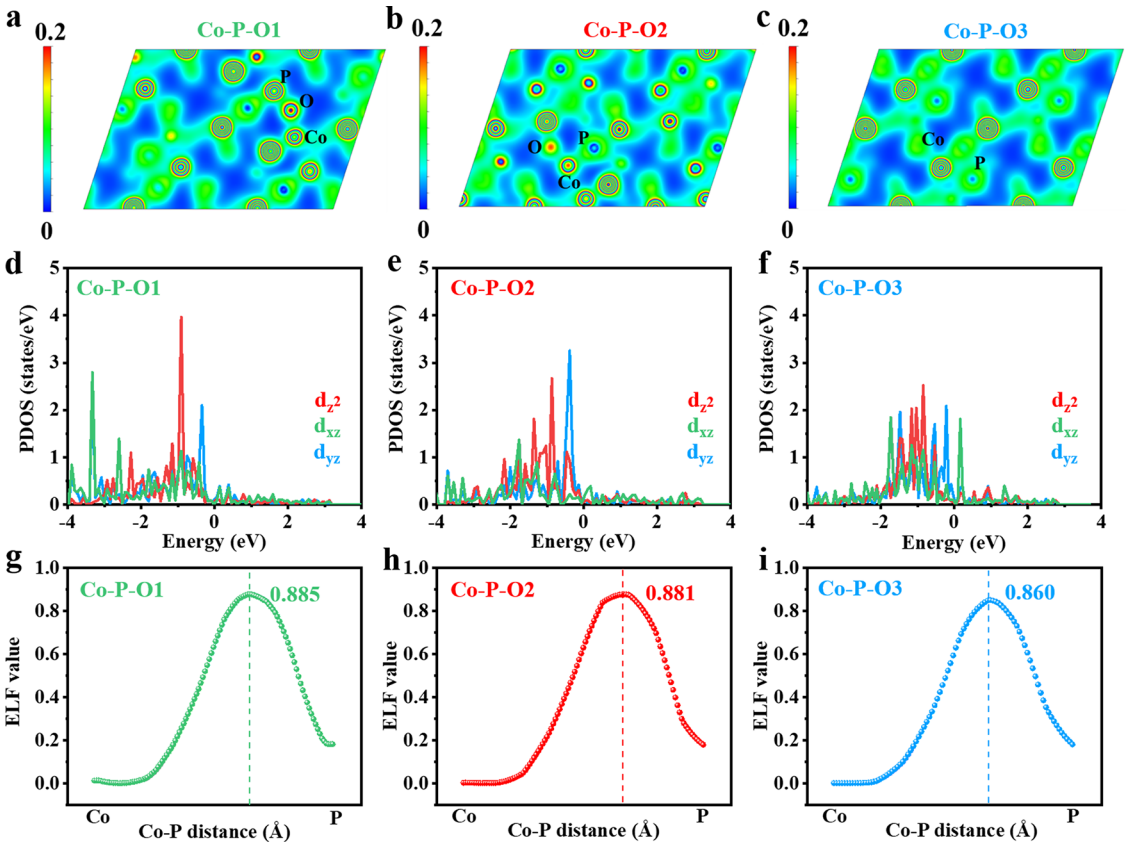

Figure 5. DFT calculated charge density contour maps of (a) Co−P−O1, (b) Co−P−O2, and (c) Co−P−O3 (red region indicates charge accumulation; blue region indicates charge depletion). Computed PDOS of the Co atom at the adsorption site for (d) Co−P−O1, (e) Co−P−O2, and (f) Co−P−O3. (g−i) ELF profile along the interatomic axes of Co and P.

Moreover, XPS analysis reveals that the distribution of elements on the surface changes and particularly that all peaks in the high-resolution XPS spectra in the Co 2p, P 2p, and O 1s regions associated with metal phosphides disappear completely (Figure S19). These observations suggest that Co oxides or hydroxides formed in situ are the real catalytic active site species for the OER or HER and that leaching of surface metal cations takes place during the OER (Figure S19a). Moreover, the P 2p signal becomes weak, showing that Co−O is generated by phosphate etching on the surface of the catalyst during the OER/HER process (Figure S19b). Changes occurring in the O 1s spectrum of Co−P−O show that a large amount of lattice oxygen is generated during the electrocatalytic process, which further confirms the loss of P and the formation of metal oxides or hydroxides (Figure S19c). ICP-AES results also show that phosphorus is leached from Co−P−O2 (Table S11). Therefore, it can be concluded that during the overall water splitting process in alkaline media, the surface of Co−P−O2 undergoes oxidation to form polyphosphates and amorphous species.

Insight into the inner mechanism for the enhanced HER and OER activity of Co−P−O2 was obtained by using DFT calculations. Considering the complexity of catalyst modeling after reconstruction, we only study the catalyst in the initial state of the reaction, where the structure models are built from our as-prepared phosphide catalysts according to previous XRD, TEM, and XPS results. In our initial catalyst reaction mechanistic considerations, the phosphorus atom is replaced by oxygen in the lattice during the construction of Co−P−O1, Co−P−O2, and Co−P−O3 (Figure S8). The DFT results (Figure 5a−c) indicate that a clear difference exists in the charge density distribution of Co−P−O2, pristine Co−P−O3, and Co−P−O1. This observation suggests that O doping into the pristine lattice greatly influences the valence states of Co atoms near O atoms owing to the greater electronegativity of O compared to P. Electronic configuration changes were further analyzed by using density of states (DOS) calculations.[45] The projected DOS (PDOS) reveals that the regulation of the relative content of the O atoms adjusts the delocalization of 3d electrons, which facilitates Co−O bond formation by overlap of Co 3d orbitals (d_{xz}, d_{yz}, and d_{z^2}) with O 2p orbitals (Figure 5d−f). Notably, due to the symmetry conservation of the octahedral field, the interactions between the $d_{x^2-y^2}$ and d_{xy} orbitals of the metal ion and the orbitals of the adsorbed intermediates during the HER/OER are negligible.[46] Hence, neither $d_{x^2-y^2}$ nor d_{xy} is shown in the above figure. Electron localization function (ELF) results of Co−P−O1, Co−P−O2, and Co−P−O3 are shown in Figure 5g−i. The ELF results indicate that the electronic structure of the Co−P bond is more active and delocalized when oxygen atoms are incorporated into pure CoP.[47] In general, the polarization and rearrangement of overall surface charge and delocalization effects of d electrons would be enhanced with the introduction of O, while excessive oxygen content would be unfavorable to the adsorption of the reactant.[48] Thus, the appropriate oxygen content in Co−P−O2 could optimize the adsorption of H_2O/OH^- and the desorption of H_2/O_2 for enhancing HER and OER activities in alkaline conditions.

To understand the origin of the excellent HER and OER performance of Co−P−O2, the free energy diagram of its

https://doi.org/10.1021/acscatal.3c04067
ACS Catal. 2023, 13, 14802−14812

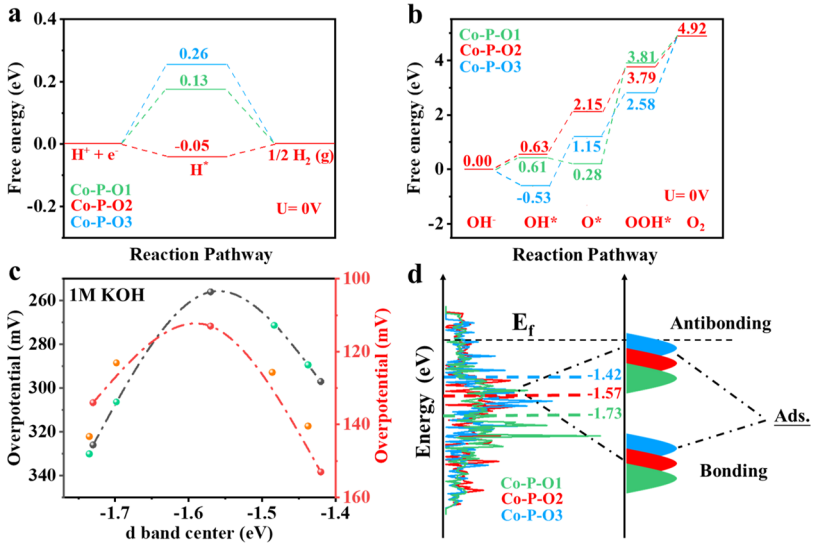

Figure 6. Gibbs free energy diagrams for Co−P−O1, Co−P−O2, and Co−P−O3 in the (a) HER and (b) OER. (c) Relationships between overpotentials and d-band centers for Co−P−O1, Co−P−O2, and Co−P−O3, Co−P−O2−80 min, Co−P−O2−100 min, Co−P−O2−140 min, and Co−P−O2−160 min (black and red points indicate calculated OER and HER d-band centers, respectively; green and orange indicate conjectural OER and HER d-band centers, respectively). (d) The DOS of Co−P−O1, Co−P−O2, and Co−P−O3 as well as the corresponding schematic illustration for noncovalent bond formation between the reaction surface and adsorbate (ads.). The d-band centers are also highlighted in the DOS curves.

(211) basal plane along with those of Co−P−O1 and Co−P−O3 was generated (Figure 6a,b). The calculated Gibbs free energy changes for the HER processes catalyzed by Co−P−O2, Co−P−O1, and Co−P−O3 are −0.05, 0.13, and 0.26 eV, respectively (Figure 6a). According to Sabatier's principle,[49] as the adsorption energy approaches zero, the catalytic reaction becomes more favorable, which indicates that the HER activity of Co−P−O2 is enhanced by changes taking place in the surface electronic structure to optimize the adsorption and desorption of H intermediates. Step 4 (formation of O_2 from OOH*) in the pathway for the OER catalyzed by Co−P−O3 (Figure 6b) has the highest free energy change, indicating that it is rate-determining. P substitution by O to produce Co−P−O1 and Co−P−O2 causes step 3 (formation of OOH* from O*) to become rate-determining. This trend indicates that appropriate O-substitution in Co−P−O2 effectively decreases the free energy of the rate-determining step during the OER process.

A plot of overpotentials vs calculated d-band center (E_d) values for the Co−P-based catalysts has a volcano shape (Figure 6c), which is widely used to assess the adsorption energy of adsorbents.[50] Co−P−O2 is at the top of the volcano plot, showing that it has the best HER and OER activity. To further confirm the regularity of the volcano-shaped plot, four comparison experiments were performed by regulating the phosphorization time in the synthesis of Co−P−O2 (Figure S20), and the overpotential of the comparison samples (Co−P−O2−80 min, Co−P−O2−100 min, Co−P−O2−140 min, Co−P−O2−160 min; the time after Co−P−O2 means the phosphating time) for HER/OER corresponds well to the trend of the volcano diagram. It is important to point out that the fitting rules for constructing the volcano diagram include fitting the measured HER and OER overpotentials of Co−P−O1, Co−P−O2, and Co−P−O3, as well as the d-band centers calculated using DFT (black points indicate OER; red points indicate HER). Then, the overpotential values for the OER at 10 mA cm^{-2} of Co−P−O2−80 min, Co−P−O2−100 min, Co−P−O2−140 min, and Co−P−O2−160 min were fitted to the volcano diagram to determine the location of their d-band centers (green points indicate OER). Impressively, the points formed by using the newly determined d-band center and the measured value of the HER were further fitted to the volcano diagram (orange points indicate HER), where the obtained results demonstrate the accuracy of the volcano diagram. Thus, it can be inferred that a moderate adjustment in the E_d energy level could lead to a balance between the adsorption and desorption capacities of intermediates. Impressively, E_d values of Co−P−O1, Co−P−O2, and Co−P−O3 relative to the Fermi level (E_f) are −1.73, −1.57, and −1.42 eV, respectively (Figure 6d), which clearly shows that O incorporation causes the d-band center of Co−P−O1 and Co−P−O2 to become more remote from the Fermi level, facilitating desorption of H_2/O_2. However, a good catalyst often requires appropriate adsorption and desorption capacity,[51] so the excessive O incorporation of Co−P−O1 will lead to unfavorable adsorption of the reactant. Notably, the wave function of antibonding states plays a dominant role in the catalytic process,[52] while the upshift of the Co−P−O2 hybridization valence band center compared to Co−P−O1 will correspondingly promote the antibonding level, which thus will improve the strong adsorption capacity due to less electron-filling antibonding states.

■ CONCLUSIONS

In summary, in the above investigation, we prepared a series of Co−P-based catalysts that possess hierarchical porous structures and atomic-level n-p effects that facilitate directed mass and electron transfer in overall water splitting in an alkaline aqueous solution. The experimental results arising from the investigation along with DFT simulations show that an appropriate level of O incorporation into the CoP lattice significantly modulates ECSA, conductivity, and d-electron structure. The Co−P−O2 nanocrystals with an optimized level of O incorporation exhibited efficient bifunctional performance

https://doi.org/10.1021/acscatal.3c04067
ACS Catal. 2023, 13, 14802−14812

in the alkaline electrolyte, requiring overpotentials of 113 and 256 mV to deliver a current density of 10 mA cm^{-2} for the HER and OER, respectively. The methods and concepts in this effort may shed new light on the future design of high-performance electrocatalysts.

■ ASSOCIATED CONTENT

Supporting Information

The Supporting Information is available free of charge at https://pubs.acs.org/doi/10.1021/acscatal.3c04067.

Additional experimental details, characterization methods, electrochemical measurements and calculation methods, supporting figures including SEM images, TEM images, optical photo, XRD patterns, XPS spectra, nitrogen adsorption and desorption isotherms, optimized structure models, electrochemical performance, supplementary tables and supplementary notes (PDF)

■ AUTHOR INFORMATION

Corresponding Authors

Jie Ying − *School of Chemical Engineering and Technology, Sun Yat-sen University, Zhuhai 519082, China;* orcid.org/0000-0002-5747-4915; Email: yingj5@mail.sysu.edu.cn

Xiao-Yu Yang − *State Key Laboratory of Advanced Technology for Materials Synthesis and Processing & School of Materials Science and Engineering & Shenzhen Research Institute & Laoshan Laboratory, Wuhan University of Technology, Wuhan 430070, China;* orcid.org/0000-0002-0880-9790; Email: xyyang@whut.edu.cn

Authors

Jiang-Bo Chen − *State Key Laboratory of Advanced Technology for Materials Synthesis and Processing & School of Materials Science and Engineering & Shenzhen Research Institute & Laoshan Laboratory, Wuhan University of Technology, Wuhan 430070, China*

Yu-Xuan Xiao − *School of Chemical Engineering and Technology, Sun Yat-sen University, Zhuhai 519082, China*

Ge Tian − *State Key Laboratory of Advanced Technology for Materials Synthesis and Processing & School of Materials Science and Engineering & Shenzhen Research Institute & Laoshan Laboratory, Wuhan University of Technology, Wuhan 430070, China*

Yuan Dong − *State Key Laboratory of Advanced Technology for Materials Synthesis and Processing & School of Materials Science and Engineering & Shenzhen Research Institute & Laoshan Laboratory, Wuhan University of Technology, Wuhan 430070, China*

Ling Shen − *State Key Laboratory of Advanced Technology for Materials Synthesis and Processing & School of Materials Science and Engineering & Shenzhen Research Institute & Laoshan Laboratory, Wuhan University of Technology, Wuhan 430070, China*

Susana I. Córdoba de Torresi − *Instituto de Química, Universidade de Sao Paulo, 05508-080 São Paulo, SP, Brazil;* orcid.org/0000-0003-3290-172X

Mark D. Symes − *WestCHEM, School of Chemistry, University of Glasgow, Glasgow G12 8QQ, United Kingdom;* orcid.org/0000-0001-8067-5240

Christoph Janiak − *Institut für Anorganische Chemie und Strukturchemie, Heinrich-Heine-Universität Düsseldorf, Düsseldorf 40204, Germany;* orcid.org/0000-0002-6288-9605

Complete contact information is available at: https://pubs.acs.org/10.1021/acscatal.3c04067

Author Contributions

J.B.C did the experiments of synthesis, electrocatalytic performance, and DFT calculation. J.Y. and X.Y.Y. conceived the project and provided the idea. J.B.C., Y.X.X., and J.Y. designed the experiments and analyzed the data. G.T. performed the TEM and EDS characterizations. Y.D. and L.S. helped with drawing pictures. J.B.C., J.Y., and X.Y.Y. wrote and revised the paper. S.I.C.T., M.D.S., and C.J. revised the paper. All of the authors discussed results and have given approval to the final version of the manuscript.

Notes

The authors declare no competing financial interest.

■ ACKNOWLEDGMENTS

This work was supported by the National Key Research and Development Program of China (2022YFB3805600, 2022YFB3805604, 2022YFB3806800), National Natural Science Foundation of China (22293020, 52201286), National 111 project (B20002), Program for Innovative Research Team in University of Ministry of Education of China (IRT_15R52), Guangdong Basic and Applied Basic Research Foundation (2021A1515111131, 2022A1515011905, 2022A1515010137, 2022A1515010504), Shenzhen Science and Technology Program (GJHZ20210705143204014, JCYJ20210324142010029, KCXFZ20211020170006010), China Postdoctoral Science Foundation (2023M732722), the Major Science and Technology Program of Hubei Province (2023BAA003), Hubei Province Key Research and Development Program (2023BAB101), Fundamental Research Funds for the Central Universities (WUT: 2023IVA095, 2023IV030h, 2023IVB086), and Jilin Province Science and Technology Development Plan (20220101248JC). The authors thank the Nanostructure Research Centre (NRC) for performing the TEM imaging. MDS thanks the Royal Society for a University Research Fellowship (URF\R\211007).

■ REFERENCES

(1) Seh, Z. W.; Kibsgaard, J.; Dickens, C. F.; Chorkendorff, I.; Norskov, J. K.; Jaramillo, T. F. Combining theory and experiment in electrocatalysis: Insights into materials design. *Science* **2017**, *355*, No. eaad4998.

(2) Zhou, Y.; Jin, N.; Ma, Y.; Cui, Y.; Wang, L.; Kwon, Y.; Lee, W. K.; Zhang, W.; Ge, H.; Zhang, J. Tube-Sponge-Inspired Hierarchical Electrocatalysts with Boosted Mass and Electron Transfer for Efficient Oxygen Evolution. *Adv. Mater.* **2023**, *35*, No. e2209500.

(3) Liu, H.; Guan, J.; Yang, S.; Yu, Y.; Shao, R.; Zhang, Z.; Dou, M.; Wang, F.; Xu, Q. Metal-Organic-Framework-Derived Co_2P Nanoparticle/Multi-Doped Porous Carbon as a Trifunctional Electrocatalyst. *Adv. Mater.* **2020**, *32*, No. e2003649.

(4) Paul, R.; Zhai, Q.; Roy, A. K.; Dai, L. Charge Transfer of Carbon Nanomaterials for Efficient Metal-Free Electrocatalysis. *Interdiscip. Mater.* **2022**, *1*, 28−50.

(5) Ying, J.; Symes, M. D.; Yang, X. Y. Directional transport for efficient catalysis. *Matter* **2023**, *6*, 674−676.

(6) Zhang, L.; Zhu, J. W.; Li, X.; Mu, S. C.; Verpoort, F.; Xue, J. M.; Kou, Z. K.; Wang, J. Nurturing the Marriages of Single Atoms with Atomic Clusters and Nanoparticles for Better Heterogeneous Electrocatalysis. *Interdiscip. Mater.* **2022**, *1*, 51−87.

(7) Wang, L.; Zhang, L.; Ma, W.; Wan, H.; Zhang, X.; Zhang, X.; Jiang, S.; Zheng, J. Y.; Zhou, Z. In Situ Anchoring Massive Isolated Pt Atoms at Cationic Vacancies of α-$Ni_xFe_{1-x}(OH)_2$ to Regulate the Electronic Structure for Overall Water Splitting. *Adv. Funct. Mater.* **2022**, *32*, No. 2203342.
(8) Zhao, S.; Lu, X.; Wang, L.; Gale, J.; Amal, R. Carbon-Based Metal-Free Catalysts for Electrocatalytic Reduction of Nitrogen for Synthesis of Ammonia at Ambient Conditions. *Adv. Mater.* **2019**, *31*, No. e1805367.
(9) Ying, J.; Lenaerts, S.; Symes, M. D.; Yang, X. Y. Hierarchical Design in Nanoporous Metals. *Adv. Sci.* **2022**, *9*, No. e2106117.
(10) Chen, J. B.; Ying, J.; Xiao, Y. X.; Dong, Y.; Ozoemena, K. I.; Lenaerts, S.; Yang, X. Y. Stoichiometry Design in Hierarchical CoNiFe Phosphide for Highly Efficient Water Oxidation. *Sci. China. Mater.* **2022**, *65*, 2685−2693.
(11) Xiao, Y. X.; Ying, J.; Tian, G.; Zhang, X. Q.; Janiak, C.; Ozoemena, K. I.; Yang, X. Y. PtPd Hollow Nanocubes with Enhanced Alloy Effect and Active Facets for Efficient Methanol Oxidation Reaction. *Chem. Commun.* **2021**, *57*, 986−989.
(12) Gao, L.; Cui, X.; Sewell, C. D.; Li, J.; Lin, Z. Recent Advances in Activating Surface Reconstruction for the High-Efficiency Oxygen Evolution Reaction. *Chem. Soc. Rev.* **2021**, *50*, 8428−8469.
(13) Ge, J.; Zheng, J. Y.; Zhang, J.; Jiang, S.; Zhang, L.; Wan, H.; Wang, L.; Ma, W.; Zhou, Z.; Ma, R. Controllable Atomic Defect Engineering in Layered $Ni_xFe_{1-x}(OH)_2$ Nanosheets for Electrochemical Overall Water Splitting. *J. Mater. Chem. A* **2021**, *9*, 14432−14443.
(14) Xiao, M. L.; Zhu, J. B.; Li, S.; Li, G. R.; Liu, W. W.; Deng, Y. P.; Bai, Z. Y.; Ma, L.; Feng, M.; Wu, T. P.; Su, D.; Lu, J.; Yu, A. P.; Chen, Z. W. 3d-Orbital Occupancy Regulated Ir-Co Atomic Pair toward Superior Bifunctional Oxygen Electrocatalysis. *ACS Catal.* **2021**, *11*, 8837−8846.
(15) Xiao, Y. X.; Ying, J.; Tian, G.; Tao, Y.; Wei, H.; Fan, S. Y.; Sun, Z. H.; Zou, W. J.; Hu, J.; Chang, G. G.; Li, W.; Yang, X. Y.; Janiak, C. Highly Dispersed PtPd on Graphitic Nanofibers and Its Heavy d-π Effect. *Appl. Catal., B* **2019**, *259*, No. 118080.
(16) Jiang, Y. L.; Yuan, L.; Wang, X. Y.; Zhang, W.; Liu, J. H.; Wu, X. F.; Huang, K. K.; Li, Y. F.; Liu, Z. P.; Feng, S. H. Jahn-Teller Disproportionation Induced Exfoliation of Unit-Cell Scale ϵ-MnO_2. *Angew. Chem., Int. Ed.* **2020**, *59*, 22659−22666.
(17) Chen, Q. X.; Liu, Y. H.; He, Z.; Wang, J. L.; Liu, J. W.; Jiang, H. J.; Huang, W. R.; Gao, G. Y.; Hou, Z. H.; Yu, S. H. Microchemical Engineering in a 3D Ordered Channel Enhances Electrocatalysis. *J. Am. Chem. Soc.* **2021**, *143*, 12600−12608.
(18) Xiao, Y. X.; Ying, J.; Tian, G.; Yang, X.; Zhang, Y. X.; Chen, J. B.; Wang, Y.; Symes, M. D.; Ozoemena, K. I.; Wu, J.; Yang, X. Y. Hierarchically Fractal PtPdCu Sponges and their Directed Mass- and Electron-Transfer Effects. *Nano Lett.* **2021**, *21*, 7870−7878.
(19) He, K.; Tadesse Tsega, T.; Liu, X.; Zai, J.; Li, X. H.; Liu, X.; Li, W.; Ali, N.; Qian, X. Utilizing the Space-Charge Region of the FeNi-LDH/CoP p-n Junction to Promote Performance in Oxygen Evolution Electrocatalysis. *Angew. Chem., Int. Ed.* **2019**, *58*, 11903−11909.
(20) Liu, Z.; Wang, L.; Yu, X.; Zhang, J.; Yang, R.; Zhang, X.; Ji, Y.; Wu, M.; Deng, L.; Li, L.; Wang, Z. L. Piezoelectric-Effect-Enhanced Full-Spectrum Photoelectrocatalysis in p-n Heterojunction. *Adv. Funct. Mater.* **2019**, *29* (41), No. 1807279.
(21) Zhang, S.; Tan, C.; Yan, R.; Zou, X.; Hu, F. L.; Mi, Y.; Yan, C.; Zhao, S. Constructing Built-in Electric Field in Heterogeneous Nanowire Arrays for Efficient Overall Water Electrolysis. *Angew. Chem., Int. Ed.* **2023**, *62*, No. e202302795.
(22) Gu, M.; Jiang, L.; Zhao, S.; Wang, H.; Lin, M.; Deng, X.; Huang, X.; Gao, A.; Liu, X.; Sun, P.; Zhang, X. Deciphering the Space Charge Effect of the p-n Junction between Copper Sulfides and Molybdenum Selenides for Efficient Water Electrolysis in a Wide pH Range. *ACS Nano* **2022**, *16*, 15425−15439.
(23) Hu, J.; Al-Salihy, A.; Wang, J.; Li, X.; Fu, Y.; Li, Z.; Han, X.; Song, B.; Xu, P. Improved Interface Charge Transfer and Redistribution in CuO-CoOOH p-n Heterojunction Nanoarray Electrocatalyst for Enhanced Oxygen Evolution Reaction. *Adv. Sci.* **2021**, *8*, No. e2103314.
(24) Wu, Y.; Liu, X.; Zhang, H.; Li, J.; Zhou, M.; Li, L.; Wang, Y. Atomic Sandwiched p-n Homojunctions. *Angew. Chem., Int. Ed.* **2021**, *60*, 3487−3492.
(25) Zhao, Y.; Dongfang, N.; Triana, C. A.; Huang, C.; Erni, R.; Wan, W.; Li, J.; Stoian, D.; Pan, L.; Zhang, P.; Lan, J.; Iannuzzi, M.; Patzke, G. R. Dynamics and Control of Active Sites in Hierarchically Nanostructured Cobalt Phosphide/Chalcogenide-Based Electrocatalysts for Water Splitting. *Energy. Environ. Sci.* **2022**, *15*, 727−739.
(26) Cao, E.; Chen, Z.; Wu, H.; Yu, P.; Wang, Y.; Xiao, F.; Chen, S.; Du, S.; Xie, Y.; Wu, Y.; Ren, Z. Boron-Induced Electronic-Structure Reformation of CoP Nanoparticles Drives Enhanced pH-Universal Hydrogen Evolution. *Angew. Chem., Int. Ed.* **2020**, *59*, 4154−4160.
(27) Hao, J.; Zhuang, Z.; Cao, K.; Gao, G.; Wang, C.; Lai, F.; Lu, S.; Ma, P.; Dong, W.; Liu, T.; Du, M.; Zhu, H. Unraveling the Electronegativity-Dominated Intermediate Adsorption on High-Entropy Alloy Electrocatalysts. *Nat. Commun.* **2022**, *13*, No. 2662.
(28) Liu, C.; Zhang, G.; Yu, L.; Qu, J.; Liu, H. Oxygen Doping to Optimize Atomic Hydrogen Binding Energy on NiCoP for Highly Efficient Hydrogen Evolution. *Small* **2018**, *14*, No. e1800421.
(29) Wang, H.; Zhai, T. T.; Wu, Y. F.; Zhou, T.; Zhou, B. B.; Shang, C. X.; Guo, Z. X. High-Valence Oxides for High Performance Oxygen Evolution Electrocatalysis. *Adv. Sci.* **2023**, *10*, No. 2301706.
(30) Li, F.; Han, G. F.; Noh, H. J.; Jeon, J. P.; Ahmad, I.; Chen, S. S.; Yang, C.; Bu, Y. F.; Fu, Z. P.; Lu, Y. L.; Baek, J. B. Balancing Hydrogen Adsorption/Desorption by Orbital Modulation for Efficient Hydrogen Evolution Catalysis. *Nat. Commun.* **2019**, *10*, No. 4060.
(31) Lv, X.; Li, X.; Yang, C.; Ding, X.; Zhang, Y.; Zheng, Y. Z.; Li, S.; Sun, X.; Tao, X. Large-Size, Porous, Ultrathin NiCoP Nanosheets for Efficient Electro/Photocatalytic Water Splitting. *Adv. Funct. Mater.* **2020**, *30*, No. 1910830.
(32) Wang, X.; Pan, Z.; Chu, X.; Huang, K.; Cong, Y.; Cao, R.; Sarangi, R.; Li, L.; Li, G.; Feng, S. Atomic-Scale Insights into Surface Lattice Oxygen Activation at the Spinel/Perovskite interface of $Co_3O_4/La_{0.3}Sr_{0.7}CoO_3$. *Angew. Chem., Int. Ed.* **2019**, *58*, 11720−11725.
(33) Lu, H.; Zhao, Y. M.; Saji, S. E.; Yin, X.; Wibowo, A.; Tang, C. S.; Xi, S.; Cao, P.; Tebyetekerwa, M.; Liu, B.; Heggen, M.; Dunin-Borkowski, R. E.; Tricoli, A.; Wee, A. T. S.; Nguyen, H. T.; Yan, Q. B.; Yin, Z. All Room-Temperature Synthesis, N_2 Photofixation and Reactivation Over 2D Cobalt Oxides. *Appl. Catal., B* **2022**, *304*, No. 121001.
(34) Yue, X.; Yi, S.; Wang, R.; Zhang, Z.; Qiu, S. Cobalt Phosphide Modified Titanium Oxide Nanophotocatalysts with Significantly Enhanced Photocatalytic Hydrogen Evolution from Water Splitting. *Small* **2017**, *13*, No. 1603301.
(35) Liu, Y.; Chen, Y.; Tian, Y.; Sakthivel, T.; Liu, H.; Guo, S.; Zeng, H.; Dai, Z. Synergizing Hydrogen Spillover and Deprotonation by the Internal Polarization Field in a $MoS_2/NiPS_3$ Vertical Heterostructure for Boosted Water Electrolysis. *Adv. Mater.* **2022**, *34*, No. e2203615.
(36) Wu, Y. J.; Yang, J.; Tu, T. X.; Li, W. Q.; Zhang, P. F.; Zhou, Y.; Li, J. F.; Li, J. T.; Sun, S. G. Evolution of Cationic Vacancy Defects: A Motif for Surface Restructuration of OER Precatalyst. *Angew. Chem., Int. Ed.* **2021**, *60*, 26829−26836.
(37) Dong, Y.; Chen, J. B.; Ying, J.; Xiao, Y. X.; Tian, G.; Symes, M. D.; Yang, X. Y. Efficient Water Dissociation on Confined Ultrafine Pt via Pyridinic N-Enhanced Heavy d-π Interaction. *Chem. Mater.* **2022**, *34*, 8271−8279.
(38) Ying, J.; Chen, J. B.; Xiao, Y. X.; Cordoba de Torresi, S. I.; Ozoemena, K. I.; Yang, X. Y. Recent Advances in Ru-Based Electrocatalysts for Oxygen Evolution Reaction. *J. Mater. Chem. A* **2023**, *11*, 1634−1650.
(39) Xiao, Y. X.; Ying, J.; Chen, J. B.; Dong, Y.; Yang, X.; Tian, G.; Wu, J.; Janiak, C.; Ozoemena, K. I.; Yang, X. Y. Confined Ultrafine Pt in Porous Carbon Fibers and Their N-Enhanced Heavy d-π Effect. *Chem. Mater.* **2022**, *34*, 3705−3714.

(40) Zhou, G. Y.; Li, M.; Li, Y. L.; Dong, H.; Sun, D. M.; Liu, X. E.; Xu, L.; Tian, Z. Q.; Tang, Y. W. Regulating the Electronic Structure of CoP Nanosheets by O Incorporation for High-Efficiency Electrochemical Overall Water Splitting. *Adv. Funct. Mater.* **2020**, *30*, No. 1905252.
(41) Lu, X. F.; Yu, L.; Zhang, J.; Lou, X. W. D. Ultrafine Dual-Phased Carbide Nanocrystals Confined in Porous Nitrogen-Doped Carbon Dodecahedrons for Efficient Hydrogen Evolution Reaction. *Adv. Mater.* **2019**, *31*, No. e1900699.
(42) Li, H. R.; Han, X. B.; Jiang, S. Y.; Zhang, L. L.; Ma, W.; Ma, R. Z.; Zhou, Z. Controllable Fabrication and Structure Evolution of Hierarchical 1T-MoS_2 Nanospheres for Efficient Hydrogen Evolution. *Green Energy Environ.* **2022**, *7*, 314−323.
(43) Ying, J.; He, Z. Z.; Chen, J. B.; Xiao, Y. X.; Yang, X. Y. Elevating the d-Band Center of Ni_3S_2 Nanosheets by Fe Incorporation to Boost the Oxygen Evolution Reaction. *Langmuir* **2023**, *39*, 5375−5383.
(44) Ji, P.; Yu, R.; Wang, P.; Pan, X.; Jin, H.; Zheng, D.; Chen, D.; Zhu, J.; Pu, Z.; Wu, J.; Mu, S. Ultra-Fast and In-Depth Reconstruction of Transition Metal Fluorides in Electrocatalytic Hydrogen Evolution Processes. *Adv. Sci.* **2021**, *9*, No. 2103567.
(45) Shin, H.; Xiao, H.; Goddard, W. A. In Silico Discovery of New Dopants for Fe-Doped Ni Oxyhydroxide ($Ni_{1-x}Fe_xOOH$) Catalysts for Oxygen Evolution Reaction. *J. Am. Chem. Soc.* **2018**, *140*, 6745−6748.
(46) Sun, Y.; Sun, S.; Yang, H.; Xi, S.; Gracia, J.; Xu, Z. J. Spin-Related Electron Transfer and Orbital Interactions in Oxygen Electrocatalysis. *Adv. Mater.* **2020**, *32*, No. e2003297.
(47) Li, Z.; Lu, X.; Zhao, R.; Ji, S.; Zhang, M.; Horton, J. H.; Wang, Y.; Xu, Q.; Zhu, J. A Heterogeneous Single Atom Cobalt Catalyst for Highly Efficient Acceptorless Dehydrogenative Coupling Reactions. *Small* **2023**, *19*, No. e2207941.
(48) Yan, X. Y.; Wang, B. B.; Ren, J.; Long, X. J.; Yang, D. J. An Unsaturated Bond Strategy to Regulate Active Centers of Metal-Free Covalent Organic Frameworks for Efficient Oxygen Reduction. *Angew. Chem., Int. Ed.* **2022**, *61*, No. e202209583.
(49) Zhu, L.; Lin, H.; Li, Y.; Liao, F.; Lifshitz, Y.; Sheng, M.; Lee, S. T.; Shao, M. A Rhodium/Silicon Co-Electrocatalyst Design Concept to Surpass Platinum Hydrogen Evolution Activity at High Overpotentials. *Nat. Commun.* **2016**, *7*, No. 12272.
(50) Shah, K.; Dai, R.; Mateen, M.; Hassan, Z.; Zhuang, Z.; Liu, C.; Israr, M.; Cheong, W. C.; Hu, B.; Tu, R.; Zhang, C.; Chen, X.; Peng, Q.; Chen, C.; Li, Y. Cobalt Single Atom Incorporated in Ruthenium Oxide Sphere: A Robust Bifunctional Electrocatalyst for HER and OER. *Angew. Chem., Int. Ed.* **2022**, *61*, No. e202114951.
(51) Ying, J.; Xiao, Y. X.; Chen, J. B.; Hu; Z, Y.; Tian, G.; Tendeloo, G. V.; Zhang, Y. X.; Symes, M. D.; Janiak, C.; Yang, X. Y. Fractal Design of Hierarchical PtPd with Enhanced Exposed Surface Atoms for Highly Catalytic Activity and Stability. *Nano Lett.* **2023**, *23*, 7371−7378.
(52) Cai, J. Y.; Song, Y.; Zang, Y. P.; Niu, S. W.; Wu, Y. S.; Xie, Y. F.; Zheng, X. S.; Liu, Y.; Lin, Y.; Liu, X. J.; Wang, G. M.; Qian, Y. T. N-Induced Lattice Contraction Generally Boosts the Hydrogen Evolution Catalysis of P-Rich Metal Phosphides. *Sci. adv.* **2020**, *6*, No. eaaw8113.

https://doi.org/10.1021/acscatal.3c04067
ACS Catal. 2023, 13, 14802−14812